Nanoscale

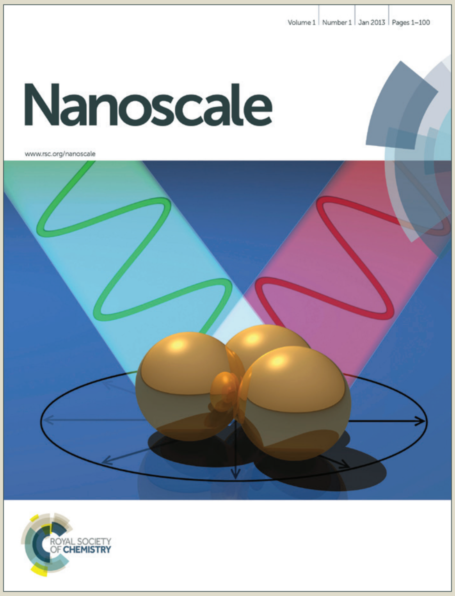

ROYAL SOCIETY OF CHEMISTRY

www.rsc.org/nanoscale

Effect of Surface Hydrogenation of Metal Oxides on the Nanomorphology and the Charge Generation Efficiency of Polymer Blend Solar Cells

Maria Vasilopoulou

Institute of Nanoscience and Nanotechnology (INN), National Centre for Scientific Research "Demokritos",
153 10, Aghia Paraskevi Attikis, Athens, Greece.

Email: mariva@imel.demokritos.gr

Abstract

In this work, the effect of surface hydrogenation of different metal oxides, in particular molybdenum and tungsten oxides widely used to enhance hole extraction and zinc and titanium oxides widely used to enhance electron extraction, on the nanomorphology and the charge generation efficiency of polymer blend solar cells, is investigated. It was found that photoactive layers based on blends using different polymers, in particular poly(3-hexythiophene) (P3HT) and poly[(9-(1-octylnonyl)-9H-carbazole-2,7-diyl)-2,5-thiophenediyl-2,1,3-benzothiadiazole-4,7-diyl-2,5-thiophenediyl] (PCDTBT), which normally differ in both morphology and electronic structure, benefited, for both polymers, from deposition on metal oxides with high surface hydrogen content, in the sense that they exhibited improved crystallinity/order as revealed from X-ray diffraction, UV-vis absorption and elipsometric measurements. As a result, increased charge generation efficiencies and reduced recombination losses were measured in solar cells using metal oxides with highly hydrogenated surfaces at bottom electrodes and based on blends of either P3HT or PCDTBT, with a fullerene acceptor, as was verified by transient photocurrent measurements. The power conversion efficiency (PCE) of those cells reached values of 4.5% and 7.2%, respectively, an increase of about 30% compared with the cells using metal oxides with low surface hydrogen content.

Key Words: Organic solar cells, surface hydrogenation, metal oxides, improved crystallinity, enhanced charge generation.

1. Introduction

In the burgeoning market of renewable energy, organic solar cells (OSCs) are becoming more attractive for large-scale, high-throughput and cost-effective manufacturing on flexible plastic substrates as they offer a viable alternative to conventional solar cells, which are fabricated via vacuum-based or high-temperature processes.[1-3] Currently, the most efficient OSC designs are based on bulk heterojunction (BHJ) structures, in which organic electron donor (D) and electron acceptor (A) materials form an interpenetrating network with the goal of optimizing photon absorption, exciton separation and charge transport.[4-8] Critical to these processes is the nanomorphology of the blend; this places a pressing challenge on the science of OSC materials and devices, as we have to be able to determine and control how the two materials mix together or segregate.[6-18] The goal of manipulating the nanomorphology of organic photovoltaic blends can be reached by using a heuristic fashion of processing approaches, namely by applying a post-annealing process, varying polymer blend ratio, solvent choice, solution concentration, film drying time and co-solvent/processing aids.[19-30] In the commonly used blend of regioregular poly(3-hexythiophene) (P3HT) and [6,6]-phenyl C_{71} butyric acid methyl ester ($PC_{71}BM$), the most effective strategy toward constructing the nanoscale D/A percolated networks with well-optimized morphology is the application of a post annealing treatment at high temperature.[18,21-24] However, devices based on the new generation donor materials which exhibit small band gap to offer a more efficient light harvesting of the solar spectrum, such as poly[(9-(1-octylnonyl)-9H-carbazole-2,7-diyl)-2,5-thiophenediyl-2,1,3-benzothiadiazole-4,7-diyl-2,5-thiophenediyl] (PCDTBT), perform better if fabricated without the post thermal annealing step.[25-27] It was found that the π-π stacking of the PCDTBT molecules is reduced upon annealing, resulting in simultaneous reduction of both the hole mobility and the device performance.[28-30] As a consequence, the ubiquitous post annealing step applied in the P3HT-based OSCs is considered prohibitive for devices using new donor materials, such as the PCDTBT copolymer. Hence, the optimization of blend nanomorphology in the devices not allowed to be heated is still a challenge.

Recently, it has also been reported that the crystalline ordering and molecular orientation of polymer donors can be tuned by modifying the surface properties of an underneath metal oxide layer.[31-33] Metal oxides with stoichiometric or non-stoichiometric compositions have been proven to be very useful as charge selective interlayers in organic solar cells.[34-43] In particular, metal oxides exhibiting intrinsic n-type conductivity, such as titanium dioxide (TiO_2) and zinc oxide (ZnO), have been utilized as electron selective interlayers,[34-38] while high work function molybdenum (MoO_x) and tungsten (WO_x) oxides are used to allow efficient hole extraction.[39-46] In each case, factors affecting the device efficiency, i.e., the metal oxide stoichiometry and work function and the energy level alignment at the metal oxide/organic interfaces, have been intensively investigated.[44-46] Reports about the dependence of photoactive blend film on the metal oxide surface properties are, however, limited.[31-33] Hydrogen, for instance, is a ubiquitous surface impurity in a plethora of metal oxides, present in many growth environments and normally being chemisorbed at their surfaces. In this paper we investigated the effect of the hydrogen (H) content of the surfaces of metal oxide underlayers on the nanomorphology of photoactive blend films and found a most startling result. Not only did the blend film nanomorphology exhibit a definite dependence on the content of H atoms in metal oxide surface adsorbates, but also this dependence was found to be universal, regardless of the type of metal oxide substrate (e. g., tungsten, molybdenum, zinc and titanium oxide) and the polymer donor (e. g., P3HT, PCDTBT). This was attributed to the epitaxial growth/texturing of the organic semiconducting layer via the formation of an extended interfacial hydrogen bonding network. Organic solar cells with different architectures and photoactive layers achieved high efficiencies, arising from the enhanced charge generation and reduced recombination losses, both being a result of the improved crystallinity/order of the polymer phase in the blend. The common element of all these devices is the intense hydrogenation of the underneath metal oxide surfaces.

2. Results and discussion

2.1. The effect of the surface hydrogen content of metal oxides on the nanomorphology of P3HT:PC_{71}BM blends. One of the main challenges of this study was to synthesize metal oxides exhibiting different amount of surface hydrogen, while keeping nearly the same chemical composition in order for them to exhibit quite similar electronic properties (such as the values of their work function and conductivity, which are both critical for device operation[39,41]). To this end, we synthesized metal oxide films, which were then subjected to a certain hydrogen annealing process. In particular, we deposited tungsten (WO_x) and molybdenum (MoO_x) oxides using a hot-wire vacuum deposition method,[43-47] zinc oxide (ZnO) using atomic layer deposition (ALD) and titanium oxide (TiO_2) following a sol-gell synthetic route (details about metal oxide synthesis are given in the experimental section). These metal oxides were then kept at 450 ^oC under 20 bar of either forming gas (FG, 90% N_2 and 10% H_2, considered as poor hydrogen environment) or pure H_2 (considered as rich hydrogen environment) for five hours. We investigated then, in detail, the effect of annealing in hydrogen containing environments on the metal oxides' composition, electronic properties and surface hydrogenation by performing X-ray (XPS) and ultraviolet (UPS) photoelectron spectroscopy, Raman and FT-IR absorption measurements, photoluminescence and conductivity measurements. According to these measurements (presented in SI as Figures S1-S3 for tungsten, Figures S4-S6 for molybdenum, Figures S7-S9 for zinc and Figures S10-S12 for titanium oxides, respectively) metal oxides subjected to annealing in environments containing different amounts of hydrogen exhibit similar chemical composition (as evidenced from Figs S1 a, S4 a, S7 a, S10 a, where the XPS core level spectra of W 4f, Mo 3d, Zn 2p and Ti 2p, respectively, are presented and discussed, while results are also summurized in Table S1) and electronic properties (similar valence band onset, midgap states and work function, as derived from the UPS spectra presented in Figs S1 c, d, S4 c, d, S7 c, d and S8 c, d). The O 1s XPS spectra, however, of the films annealed in hydrogen rich environment, as compared to hydrogen poor one, show dramatic differences. The O 1s XPS peak of metal oxides annealed in hydrogen poor environment can be resolved into two main peaks, one peak at 530.8 eV, typical for all metal oxides, and a second smaller peak at 532.3 eV, which can be assigned to adsorbed water molecules.[43,46] In the O 1s XPS spectra of metal oxides annealed in hydrogen rich environment a third peak at 531.6 eV has also a contribution, which can be attributed to hydroxyl bonded to metal surface species.[43] The presence of a higher amount of surface (and possibly bulk) hydrogen in metal oxides annealed in hydrogen rich environment was also supported by Raman, FT-IR and photoluminescence measurements (Figs S2, S3a, S5, S6a, S8, S9a, S11, S12a and relative discussion). As a result, metal oxide films exhibiting quite similar stoichiometries, electronic properties and, also, conductivities (Figs S3b, S6b, S9b, S12b), but different amounts of surface hydrogen (films annealed in FG exhibit low content of surface hydrogen and are termed hearafter as WO_x, MoO_x, ZnO and TiO_2 while films annealed in pure H_2 exhibit a high amount of surface hydrogen and termed hearafter as OH-WO_x, OH-MoO_x, OH-ZnO and OH-TiO_2), were synthesized to serve as charge selective interlayers when deposited on top of the bottom electrodes of organic solar cells. Note that the reason that FG was chosen as the hydrogen poor environment (instead of using non-H_2 inert gas such as N_2) in order to ensure the same electronic structure of the outermost film layers eg., under-stoichiometric WO_x and MoO_x would change to nearly stoichiometric oxides when annealed in N_2. The use of reducing ambient was thus deemed necessary.

We next investigated the influence of surface hydrogen content of metal oxide layers on the nanomorphology of P3HT:PC_{71}BM (1:0.8 %w/w) blend films, spin coated from solutions in chlorobenzene under identical conditions and thermally treated at 130 ^{o}C for 5 min to remove solvent residuals and allow the polymer chains to achieve a certain degree of orientation.[48,49] In order to investigate the nanomorphology of blend films deposited on various metal oxide substrates, X–ray diffraction (XRD) measurements were carried out. The corresponding XRD graphs are shown in Figures 1 a, d, g and j for P_3HT:PC_{71}BM films deposited on tungsten, molybdenum, zinc and titanium oxides, respectively, with either low or high surface hydrogen content. When deposited on metal oxides with low surface hydrogen content, P3HT:PC_{71}BM films exhibit weak diffraction patterns (diffraction angle $2\theta=5.3^{o}$, 10.7^{o} and 15.9^{o} for the primary (100), secondary (200) and tertiary (300) peaks), indicating that P3HT chains in P_3HT:PC_{71}BM films form crystallites with lamellae oriented perpendicularly to the substrate (edge-on orientation).[49] The intensity of the diffraction peaks is relatively low, which is an indication of a moderate degree of P3HT film crystallinity in all these cases. However, the situation is quite different when the P3HT:PC_{71}BM films are deposited on top of the metal oxide substrates with a high content of surface hydrogen. The characteristic diffraction peaks (h00) (h=1,2,3) of P3HT crystallites become more pronounced, indicating that the stacking perpendicular to the substrate is significantly enhanced for all films. However, despite the fact that all peaks show a clear change in intensity when blend films are deposited on top of the hydrogen-rich metal oxide surfaces indicating a higher degree of polymer crystallization, the domain size remains nearly unaffected in all these cases. Interestingly, the size of these small domains is generally on the order of the exciton diffusion length (the mean size of the polymer crystallites at (100) reflection was estimated to be ~10.60-10.97 nm by applying Scherrer's formula[48]). According to these results while the domain spacing (provided by the position of the XRD peaks) is similar in all blend P3HT:PC$_{71}$BM films, the purity and volume fraction of the domains (resulting from the different intensities of the XRD peaks) are significantly enhanced when these films are deposited on top of metal oxides with hydrogen-rich surfaces. Therefore, these XRD results support the hypothesis that surface hydrogenation of the underneath metal oxides strongly improves the intraplane chain stacking of P3HT in a direction perpendicular to the film substrate, irrespective of the metal cation. Moreover, the π-π stacking direction (010) of P3HT chains (corresponding to diffraction angle $2\theta=22.2^o$) is also seen in the blend films deposited on the metal oxides with the highly hydrogenated surfaces, which is indicative of a significant face-on packing;[50,51] this is not observed in the XRD patterns of films deposited on metal oxides with hydrogen-poor surfaces. Note that diffraction peaks caused by PC$_{71}$BM crystallites were not detected in the diffractograms of blend films irrespective of the hydrogen content of the metal oxide substrate. This is an indication that the film morphology of PC$_{71}$BM is not affected by the H content on the surface of the oxide layer. Therefore, the main result derived from the XRD study is that blend P3HT:PC$_{71}$BM films fabricated on hydrogenated metal oxide surfaces exhibit a strong enhancement of their orientation not only along the (100)-axis normal to the substrate (edge-on orientation), but also along the (010)-axis parallel to the underneath metal oxide (face-on orientation).

Figures 1 b, e, h and k present the evolution of the absorption spectra of P3HT:PC$_{71}$BM blend films when deposited on tungsten, molybdenum, zinc and titanium oxides, respectively, with either low or high hydrogen content. All films were annealed at 130 ^{o}C for 5 min, followed by quenching at room temperature and subsequent measurements. In all P3HT:PC$_{71}$BM films there is a clear vibronic structure in the P3HT absorption component in the films, but when these films are deposited on the hydrogen-rich metal oxide surfaces the P3HT vibronic structure appears more pronounced, which is in agrement with the increased amount of structural ordering/crystallinity of the P3HT phase, resulting from the XRD patterns. Note that from the steady-state photoluminescence (PL) spectra of the same films (Figure S13) it is clear that the higher surface hydrogen content of the underneath metal oxides tends to increase the PL intensity, suggesting a reduction in non-radiative quenching pathways in the more ordered/crystalline films. These effects are attributed to the higher degree of segregation of ordered P3HT domains in the blend film when it is coated on the highly hydrogenated metal oxide surfaces.

Figures 1 c, f, i, l show the deduced refractive index for the same P3HT:$PC_{71}BM$ blends when deposited on the various metal oxide surfaces. The blend films deposited on the hydrogen-poor metal oxide surfaces exhibit a less-crystaline polymer phase, seen here as a blue shifted extinction coefficient (k) and a lower intensity shoulder at 625 nm (the origin of this shoulder is directly related to crystallinity[52,53]). This result is in agreement with the XRD and absorption data, and supports the idea that deposition of P3HT:$PC_{71}BM$ blend films on highly hydrogenated metal oxide surfaces significantly increases the crystallization of the P3HT phase in the films. Note also that the change in the refractive index (n) at wavelengths well below the absorption onset can be correlated to changes in film density.[53] Consequently, an increase in film density (arising from enhancement of the volume fraction of the crystalline domains) can be concluded from the increase of the refractive index when these films are fabricated on the hydrogenated surfaces of the underneath metal oxides.

In order to interpret the enhanced crystallization of the P3HT phase in the blend films, we must take into account that the polymer is a π-conjugated system bearing polar groups (such as thienyl) in its backbone. When deposited on the metal oxide substrates, which have O-H terminated bonds in their surface, there are π-H interactions between the polar groups of the polymer backbone and the hydrogen atoms of the substrate surface. In this way, an extended network of interfacial hydrogen bonds is formed, which act as nucleation sites for interfacial crystallization. The proposed interfacial crystallization mechanism is illustated in Figure 1 m. In this case, the hydrogen bonding between the polar groups of the polymer matrices and the hydrogenated metal oxide surface could lead to strong interactions among the macromolecules and the underneath layer and, thus, facilitate the nucleation and lateral interfacial crystallization. As one molecular layer is nucleated on the hydrogenated surface, other molecules could form hydrogen bonds with the molecules already attached to the hydrogenated metal oxide surface. As a result, oriented structures of the polymer matrices on top of the hydrogenated surfaces are formed. The above mechanism could also explain the lack of crystallinity of the $PC_{71}BM$ phase in the blends; since polar groups are not present in the fullerene molecules the formation of a hydrogen bonding network between such molecules and the metal oxide surfaces is not expected.

2.2 Conventional and inverted photovoltaic cells based on P3HT:$PC_{71}BM$. We next evaluated the impact of surface hydrogenation of metal oxide substrates on the OSC performance. The conventional device structure was glass / ITO / metal oxide hole selective interlayer (20 nm) / P3HT:$PC_{71}BM$ (150 nm) / PW-12 POM electron selective interlayer (5 nm)/Al. where the metal oxide was either tungsten or molybdenum oxide, with both low and high surface hydrogen content in each case. The PW-12 POM was a previously reported electron extraction layer.[54,55] The reverse device structure was glass /FTO / metal oxide electron selective interlayer (20 nm) / P3HT:$PC_{71}BM$ (150 nm) / OH-MoO_x hole selective interlayer (10 nm) / Al, where the metal oxide was either zinc or titanium oxide, also with both low and high content of surface hydrogen in each case. In Figure 2 a the forward and reverse device architecture and the corresponding energy levels (as derived from UPS measurements shown in the SI or taken from the literature[43,46]) of bulk materials used in this study (metal oxides and organic semiconductors of the photoactive blends), are shown. The current density-voltage (J-V) characteristics under air-mass 1.5 simulated irradiance, of the cells based on P3HT:$PC_{71}BM$ blend films as photoactive layers, with both conventional and reverse architectures, are shown in Figures 2 b, c and Figures d,e, respectively. A tabular presentation of all cell operational characteristics, in particular open-circuit voltage (V_{oc}), short-circuit current (J_{sc}), fill factor (FF) and PCE along with their statistics (average out of 32 devices) is given in table S2. It is obvious that all cells show significant improvement in their V_{oc} and J_{sc} and overall PCE when incorporating photoactive layers fabricated on the hydrogen rich metal oxide surfaces. For the conventional cells, the device with a WO_x hole selective interlayer (Figure 2 b) gives a PCE of 3.2%, while the device with the OH-WO_x interlayer exhibits a PCE of 4.2% (representing a 31% improvement). Similarly, a high PCE of 4.5% was obtained from the device with the OH-MoO_x interlayer, which is improved by 32% compared with the PCE value of 3.4% for the device with the MoO_x interlayer (Figure 2 c). Similar improvements were obtained in all reverse devices based on P3HT:$PC_{71}BM$ active layers when incorporating the metal oxides with the highly hydrogenated surfaces; a PCE=4.4% was calculated for the device with the OH-ZnO layer compared with the PCE=3.4 % for the one with the ZnO interlayer (Figure 2 d), and a PCE=4.2% was estimated for the device with the OH-TiO_2 interlayer, compared with the PCE=3.3 % for the one with the TiO_2 interlayer (Figure 2 e). The above enhancement in the PCE of all OSCs incorporating the metal oxides with a high surface hydrogen content is mainly a result of the significant improvement in J_{sc} and V_{oc} for those devices, as illustrated in Figures 2 f and g, respectively. Regarding this improvement, it is well known that J_{sc} is related to the device quantum efficiency, which in turn depends on the light absorption capacity and the charge transport properties of the organic semiconductor. The enhanced crystallinity of the P3HT phase in the blend films fabricated on metal oxides with highly hydrogenated surfaces influences both the optical absorption of the films (as shown in Figure 1) and their charge transport properties,[18] and is capable of explaining the large increase in J_{sc}.

The incident photon-to-current-conversion efficiency (IPCE) spectra of the solar cells are shown in Figure 3. It is obvious that all devices incorporating metal oxides with highly hydrogenated surfaces show increased IPCE over the entire wavelength range when compared to their counterparts with metal oxides exhibiting hydrogen poor surfaces. The average IPCE peak between 450-550 nm is nearly 60% for the latter devices, while it jumps to more than 75% for the former devices. The nearly 25% increase in the IPCE of all devices is consinstent with the improvement in the J_{sc} of those devices and can be explained by the significant differences in the crystallization of the P3HT phase of the blend films when fabricated on the OH-metal oxide surfaces. Note that the increase in the FF of the cells (table S2) also arises from the enhancement in polymer organization, which influences the charge transport properties of the blend films.

On the other hand, the enhanced crystallinity of the P3HT phase of the blend film is not expected to have a direct impact on the V_{oc}. Generally, V_{oc} is given by the following relationship:[56]

$$V_{OC} = \left|HOMO_D\right| - \left|LUMO_A\right| - kTq \ln \frac{N_{eff}^2}{np} \qquad (1)$$

where $|HOMO_D|$ is the highest occupied molecular orbital (HOMO) of the polymer donor, $|LUMO_A|$ is the lowest unoccupied molecular orbital (LUMO) of the fullerene acceptor, k is Boltzmann's constant, T is the temperature, q is the elementary charge, N_{eff} is the effective density of states, and n and p are the concentrations of electrons and holes, respectively. From this relationship it can be deduced that V_{oc} is determined both by the energy level difference between $|HOMO_D|$ and $|LUMO_A|$ (which is not altered by the hydrogenation of the underneath metal oxide) and by the carrier concentrations. The steady-state carrier concentration is mainly influenced by the charge generation efficiency and the presence of interfacial trap states; both can be significantly influenced by the nanomorphology of the photoactive blend film.

2.3. Recombination study. In an effort to probe the charge generation and extraction dynamics in these cells, we carried out transient photocurrent (TPC) measurements, where a brief pulse of light photogenerates carriers in the solar cell. These carriers are driven towards the electrodes by the internal field of the cell. Through applying an external DC bias, we can change the internal field and we can alter the amount of time the carriers spend in the device prior to extraction. It is therefore possible to observe carrier generation, transport and recombination dynamics in these systems.[57] Figure 4 shows the TPC traces for each of the four different types of cells (with the different metal oxides exhibiting low and high surface hydrogen content in each case), while they are operating at their maximum power point (500 mV applied bias). It is obvious that the fewest carriers were extracted from the cells with the photoactive layers fabricated on the metal oxides exhibiting hydrogen poor surfaces. From the photocurrent peaks, we see that the surface hydrogenation of metal oxide substrates has the effect of seriously enhancing carrier generation, consistent with the improvement of P3HT phase crystallinity/order observed by XRD measurements. Molecular order not only increases the generation yields of mobile carriers, and also the charge separation efficiency within the photoactive layer of the cells, but also decreases the recombination rates, as charges transport through the blend film; this has a significant positive impact on device operation.

Figure 5 shows the time integral of the photocurrent trace, which gives the total number of the extracted charges as a function of time, for each of the solar cells by applying a bias at the maximum power as before, for which the internal field of the device is reduced (i. e., the internal field becomes maximum for high reverse bias). At these conditions the mobile carriers slow down and recombination limits the quantity of the extracted charge. It is obvious that in the cells with the blend photoactive films fabricated on the highly hydrogenated metal oxide surfaces the mobile carriers collected at the maximum power point are allways more numerous than those collected under the same conditions in the cells incorporating the metal oxides with the hydrogen poor surfaces. The above results indicate that the major difference between the cells fabricated on metal oxides with hydrogen poor or rich surfaces is between the initial charge generation (being higher in the latter devices) and the recombination losses (being reduced in the latter cells). As a result, a higher number of mobile carriers are extracted at the maximum power point in the devices with the blend films fabricated on OH-metal oxide surfaces.

Up to this point, we investigated the effect of the hydrogen content of the underneath metal oxide surfaces on the nanomorphology of a P3HT:$PC_{71}BM$ blend film and also on the charge generation, the recombination losses and the overall performance of conventional and reverse solar cells. Our results indicate that the P3HT phase is more crystalline/ordered in the blends fabricated on the highly hydrogenated metal oxide surfaces, which has a direct positive impact on the charge generation and recombination losses, resulting in an improved performance in these cells. However, to ensure a fair comparison we have to take into account the small, but worth mentioning, increase in conductivity of the metal oxides with the higher surface hydrogen content (Figs S3 b, S6 b, S9 b, S12 b), which may influence transport of mobile carriers transport within the metal oxide layer. An other important issue is whether the hydroxyl groups at the metal oxide/photoactive blend interface may act as charge carrier traps as reported previously for the SiO_2/organic semiconductor interface in organic transistors.[58] If this is the case here it can only strengthen our argument about the influence of metal oxides surface properties on the photoactive blend nanomorphology. However, to reveal if hydrogen introduces interface traps at the metal oxide/organic interface further investigated in needed which is beyond the scope of the present work.

2.4. The effect of surface hydrogen content of metal oxides on the nanomorphology and solar cell performance of PCDTBT:$PC_{71}BM$ blends. Noteworthily, similar results were obtained when PCDTBT:$PC_{71}BM$ blend films were spin-coated on top of metal oxides. It is well-known that PCDTBT has only weak, short-range molecular order, while, in contrast to P3HT, thermal annealing reduces the coherence length of its π-π stacking, increasing the disorder of the polymer electronic structure.[59,60] The XRD patterns of PCDTBT:$PC_{71}BM$ films deposited on different metal oxide surfaces are presented in Figures 6 a, c, e, g. These films were annealed at 70 ^{o}C for 5 min because annealing at high temperatures increases recombination losses and worsens device performance.[61] A few weak peaks which we attribute to lamellar and backbone spacings of the polymer, are present in the XRD graphs of the PCDTBT:$PC_{71}BM$ films fabricated on metal oxides with slightly hydrogenated surfaces. However, by using a high degree of surface hydrogenation of the undeneath metal oxides, we were able to construct the interpenetrating network structure of the PCDTBT:$PC_{71}BM$ system, as evidenced by the XRD graphs presented in Figure 6. A prominent broad peak at $2\theta=19.1^{o}$ arises in the XRD patterns of these films; we attribute this peak to the π-π stacking of the polymer, which is primarily oriented with its chains parallel to the substrate (face-on packing), while the broadness of this peak indicates that there is a distribution of π-π stacking orientations. A small increase in the peak at $2\theta=4.85^{o}$ also indicates improved edge-on packing, which means that the overall crystallinity of PCDTBT is improved when blend films are deposited on highly hydrogenated metal oxide surfaces. The enhanced crystallinity/order of the PCDTBT phase in the blend films, quite similar to that of the P3HT phase in its own blend, fabricated on the OH-metal oxide surfaces, was further evidenced by UV-vis absorption measurements, shown in Figures 6 b, d, f, h. All blend films exhibited a broad absorption peak, extending from 450 nm to 700 nm, which is attributed to the PCDTBT phase. The shape of the absorption peaks is unchanged; the intensity, however, is significantly increased in the spectra of blend films fabricated on the OH-metal oxide surfaces, which is an indication or improved order in these films.

Solar cells using the conventional and reverse structures were fabricated with PCDTBT:$PC_{71}BM$ blend films (with an approximate thickness of 100 nm) used as photoactive layers and with metal oxide interlayers on the bottom electrode. Results are shown in Figures 7 a, c, e, g and are summarized in table S3. It is seen that the devices with OH-metal oxides exhibit a significant increase in their operational characteristics, achieving higher efficiencies, than their counterparts with metal oxides having low surface hydrogen content. The conventional device with the WO_x anode interlayer shows a PCE of 5.6%; the one with the OH-WO_x interlayer, however, exhibits a higher PCE of 7.0% (25% improvement). Our champion device with the OH-MoO_x interlayer exhibits even higher efficiency, reaching 7.2%, which represents a 26% improvement relative to that of 5.7 % corresponding to the device with the MoO_x interayer. Similarly, a large efficiency enhancement was achieved in the reverse OSCs with the hydrogenated Zn and Ti oxide surfaces (exhibiting PCEs equal to 7.1% and 7.0%, respectively, compared with the devices using their counterparts with hydrogen poor surfaces presenting efficiencies 5.6% and 5.5%, respectively). From all these results it again becomes evident that the hydrogenation of the metal oxide surfaces lying underneath the organic photoactive layer (on the bottom eletrode) is highly critical for optimal solar cell performance. In Figures 7 b, d, f, h the IPCEs of the above devices show a pronounced evolution of their intensity when using OH-metal oxide surfaces. The enhanced structural order of PCDTBT in these devices may explain the improvement in IPCEs as a result of higher carrier photogeneration and reduced recombination losses, as discussed in the case of P3HT:$PC_{71}BM$ blend films. All the above results provide unambiguous evidence for the significant role of hydrogen incorporation on the metal oxide surface (or lattice) in solar cell performance.

3. Conclusions

In this work, a novel approach was employed to contol the crystallinity/morphology of P3HT:$PC_{71}BM$ and PCDTBT:$PC_{71}BM$ blend films. A simple hydrogenation step of the surface of metal oxide layers deposited at the bottom electrodes, to serve as charge selective interlayers in organic solar cells, was found to enhance the self-organization ability of the polymer chains into an more ordered structure consisting of a larger volume fraction of crystallites exhibiting both the edge-on and, remarkably, the face-on orientation. These optimal morphology changes were universal, regardless of the metal oxides (e. g., tungsten, molybdenum, zinc and titanium oxide) used as either hole or electron selective interlayers at the bottom electrode of conventional and reverse solar cells, respectively. The morphology change was followed by enhanced charge generation and suppressed mobile carrier recombination losses, which allowed for a substantial improvement in J_{sc}, V_{oc} and FF of the devices, resulting in high PCE values of up to 4.5% and 7.2% in P3HT:$PC_{71}BM$ and PCDTBT:$PC_{71}BM$-based devices, respectively, using hydrogenated metal oxide surfaces at the bottom electrodes.

4. Methods

Preparation of hydrogenated metal oxides: Under-stoichiometric tungsten (WO_x) and molybdenum (MoO_x) oxides were deposited, using a previously reported hot-wire vapour deposition system,[62-64] by heating a metallic filament at 560 ^{o}C in N_2 environment with a simultaneous injection of atomic hydrogen pulses. Zinc oxide (ZnO) films were deposited using an atomic layer deposition (ALD) system (LUCIDA M100, NCD). Diethyl zinc [DEZ, $Zn(C_2H_5)_{2]}$ and water (H_2O) vapor were used as the zinc precursor and reactant, respectively. The DEZ source was maintained at 10°C using a cooling circulator. The canister containing the water source was at room temperature. During deposition, Ar gas was continuously supplied to the reaction chamber at a flow rate of 100 sccm. ALD-ZnO was deposited at 1.39 Å/cycle. Titanium oxide (TiO_2) films were spin coated from their titania precursor solution, consisting of 550 µl titanium(IV) ethoxide, 375 µl conc. HCl, and 7 ml THF. Titanium(IV) ethoxide (99+%) precursor was purchased from Alfa Aesar and used as received. Afterwards, the samples were calcinated at 450 °C for 30 min. A slow heating ramp of 1.2 °C min^{-1} was found to be crucial in order to avoid cracking of the titania film due to shrinkage upon crystallisation. The hydrogenation of all metal oxide layers was performed by heating the films at 450 ^{o}C for 5 hours in either FG or pure H_2 environment

Device fabrication and characterization. Organic solar cell devices were fabricated either on indium tin oxide (ITO) or on fluorinated tin oxide (FTO) coated glass substrates (2x2 cm^2), which served as the anode and cathode electrode in devices with conventional and reverse architecture, respectively. Substrates were ultrasonically cleaned with a standard solvent regiment (15 min in deionized water, acetone and isopropanol successively). In conventional devices a W or Mo oxide layer about 20 nm thick was deposited on top of ITO on glass to serve as anode interlayer, while Zn and Ti oxide cathode interlayers with a thickness of approximately 20 nm were deposited on FTO on glass substrates, followed by the photoactive layer. The active layer consisted of either a P3HT:PC$_{71}$BM blend (1:0.8 wt.% ratio) with a concentration 20 mg/ml in chlorobenzene (resulting in a film thickness of approximately 150 nm) or a PCDTBT:PC$_{71}$BM blend (1:4 wt.% ratio) with a concentration 25 mg/ml in chlorobenzene solution (resulting in a film thickness of about 100 nm); it was spin-cast on top of the metal oxide layers at 600 and 900 rpm, respectively. After spin coating, the active layer was annealed at 130 or at 70 ºC, respectively, for 5 min in air. Then, a ~5 nm tungsten polyoxometalate (12-phosphotungstic acid, $H_3PW_{12}O_{40}$, "PW-12 POM") film was spin coated from a methanol solution to serve as the electron selective interlayer in the conventional devices, while a ~10 nm under-stoichiometric molybdenum oxide (MoO_x) film was deposited to serve as the hole selective interlayer in the devices with reverse architecture. The devices were completed with a 150 nm thick aluminum top electrode, deposited in a dedicated chamber. All chemicals were purchased from Sigma-Aldrich and used with no further purification.

Measurements and instrumentation: The crystalline phase of P3HT:PC$_{71}$BM and PCDTBT:PC$_{71}$BM films deposited on either under-stoichiometric or hydrogenated metal oxide substrates was investigated by X-ray diffractometry (XRD) (with a SIEMENS D500 diffractometer) using CuKα radiation. The measurements were performed using the following combinations of slits: 1.0°/1.0°/1.0° as aperture diaphragms, 0.15° as detector diaphragm and 0.25° as diffractor beam monochromatic diaphragm. The measured 2θ, ranging between 1° and 30°, was scanned in steps of 0.03°/5s. Film thicknesses were estimated with ellipsometry. The current density-voltage characteristics of the fabricated solar cells were measured with a Keithley 2400 source-measure unit. For V_{oc} and photocurrent measurements, devices were illuminated with a Xenon lamp and an AM1.5G filter to simulate solar light illumination conditions with an intensity of 100 mW/cm^2. To accurately define the active area of all devices we used aperture masks during the measurements with areas equal to those of the Al contacts (12.56 mm^2). The measurements were performed in air and at room temperature. Chemical analysis of all metal oxide films before and after hydrogenation was performed with XPS measurements in an ultra-high vacuum VG ESCALAB210. The spectra were obtained after excitation using Mg Kα (1,253.6 eV) radiation of a twin anode in a constant analyzer energy mode with pass energy of 30 eV. All binding energies were referred to the C 1s peak at 284.8 eV and to the O 1s peak at 530.2 eV of the surface adventitious carbon and oxygen, respectively. The stoichiometry of W and Mo oxides was estimated using the XPS-measured W 4f and Mo 3d core levels, respectively, and the corresponding O 1s core-level spectra. To this extent, the areas under the photoemission peaks were integrated by fitting the O 1s and W 4f (or Mo 3d) spectra with asymmetric Gaussian-Lorentzian curves. A qualitative estimation of the hydrogen content was performed by fitting the O 1s core levels. The raw data, after a Shirley background subtraction, were fitted by a non-linear least squares routine using peaks with a mix of Gaussian and Lorentzian shapes. The error is estimated at ± 10% in all the XPS-derived atomic percentages. Similarly, to define the Zn and Ti oxide stoichiometry the Zn 2p and Ti 2p XPS core levels, respectively, were recorded and analyzed. The valence band spectra of the metal oxides were evaluated after recording the UPS spectra of film about 10 nm thick, deposited on an ITO (or FTO) substrate, taken from the batch used for solar cell fabrication. For the UPS measurements, the He I (21.22 eV) excitation line was used. A negative bias of 12.28 V was applied to the samples during UPS measurements in order to separate the sample and analyzer high binding energy (BE) cut-offs and estimate the absolute work function value from the high BE cut-off region of the UPS spectra. The analyzer resolution is determined from the width of the Au Fermi edge to be 0.16 eV. Regarding the UPS measurements, because the high intensity UV photons used for UPS measurements may alter the surface of metal oxide films, we adopted a certain protocol for the measurement of the oxides' work function: we first measure the core levels and work function of the sample using low intensity X-rays, then we measure the work function with UPS and finally we measure again the core levels and work function with XPS to verify that the samples have remained unaffected.

Micro-Raman spectra were obtained with a Renishaw inVia Reflex microscope, using an Ar^+ ion laser (λ = 514.5 nm) as excitation source. The laser beam was focused onto the samples by means of a 50x objective lens and the laser power density was 0.4 mW/μm^2. All Raman spectra of the samples were obtained on silicon wafers. To remove the background signal, the spectrum of a clean silicon wafer was subtracted from all Raman spectra of the films. Cosmic ray lines were also removed from the spectra. Overlapped bands in specific areas of the Raman spectra were resolved using Gaussian functions to fit the data.

Absorption measurements were taken using a Perkin Elmer Lampda 40 UV/Vis spectrophotometer. The film resistance was measured using the four-point probe method with a dedicated Keithley meter. FT-IR transmittance spectra were recorded on a Bruker, Tensor 27 spectrometer using 128 scans at 4 cm^{-1}. Incident photon-to-current efficiencies (IPCE) were measured on an Autolab PGSTAT-30 potentiostat, using a 300W Xe lamp in combination with an Oriel 1/8 monochromator for dispersing the light in an area of 0.5 cm^2.

Transient photocurrent measurements were performed by photogenerating carriers in solar cells through illumination from the ITO (FTO) side by a 7 ns pulse of Nd:YAG laser (Quanta-Ray PRO-170, Spectra Physics) at 532 nm excitation wavelength. The laser system was running at a repetition rate of 2.177 Hz, and a fluence of 3.75 mW cm^{-2}. In order to improve the signal-to-noise ratio, the transient photocurrent data were obtained by an average of up to 100 measurements. The cells were biased with an Agilent 33519B waveform generator operating in DC mode.

Supporting Information

Additional Figures (XPS, UPS, FT-IR, Raman, conductivity measurements and steady-state photoluminescence spectra) are included in SI (Figures S1-S14 and tables S1-S3).

Acknowledgements

This research has been co-financed by the European Union (European Social Fund – ESF) and Greek national funds through the Operational Program "Education and Lifelong Learning" of the National Strategic Reference Framework (NSRF) - Research Funding Program: ARCHIMEDES III. The author would like to also thank Dr. D. Davazoglou, Dr. P. Argitis, Dr. D. Georgiadou, Dr. G. Papadimitropoulos, Dr. D. Kouvatsos, A. Soultati, E. Polydorou and Dr. A. Kaloudi-Chantzea for valuable support.

References

1. G. Yu, J. Gao, J. C. Hummelen, F. Wudl, A. J. Heeger, *Science*, 1995, **270**, 1789.
2. T. M. Clarke, J. R. Durrant, Chem. Rev., 2010, **110**, 6736.
3. J. Y. Kim, K. Lee, N. E. Coates, D. Moses, T. Q. Nquyen, M. Dante, A. J. Heeger, Science, 2007, **317**, 222.
4. Q. Gan, Q. F.G. Bartoli, Z. H. Kafafi, Adv. Mater., 2013, **25**, 2385.
5. G. Li, V. Shrotriya, J. Huang, Y. Yao, T. Moriarty, K. Emery, Y. Yang, Y. Nat. Mater., 2005, **4**, 864.
6. L. T. Dou, J. B. You, J. Yang, C. C. Chen, Y. J. He, S. Murase, T. Moriarty, K. Emery, G. Li, Y. Yang, Nat. Photonics, 2012, **6**, 180.
7. Y. M. Sun, G. C. Welch, W. L. Leong, C. G.Takacs, G. C. Bazan, A. J. Heeger, Nat. Mater., 2012, **11**, 44.
8. M. A. Green, K. Emery, Y. Hishikawa, W. Warta, E. D. Dunlop, Solar cell efficiency tables (Version 42) Progress in Photovoltaics: Research and Application, 2013, **21**, 1.
9. M. Aryal, K. Trivedi, W. Hu, ACS Nano, 2009, **3**, 3085.
10. N. Ning, S. Fu, W. Zhang, F. Chen, K. Wang, H. Deng, Progress in Polymer Science, 2012, **37**, 1425.
11. D. Gargi, R. J. Kline, D. M. DeLongchamp, D. A. Fisher, M. F. Toney, B. T. O’ Connor, J. Phys. Chem. C, 2013, **117**, 17421.
12. N. D. Treat, . G. Shuttle, M. F. Toney, J. G. Hawker, M. L. Chabinyc, J. Mater. Chem., 2011, **21**, 15224.
13. D. M DeLongchamp, R. J. Kline, D. A. Fisher, L. J. Richter, M. F. Toney, Adv. Mater., 2011, **23**, 319.
14. P. K. Nayak, L. Barnea-Nehoshtan,R. S. Kim, A. Shu,G. Man, A. Kahn, D. Lederman, Y. Feldman, D. Cahen, Energy Environ. Sci., 2013, **6**, 3272.

15. S. Shao, J. Liu, J. Zhang, B. Zhang, Z. Xie, Y. Geng, ACS Appl. Mater. Inter., 2012, **4**, 5704.

16. R. A. Street, J. E Northrup,. A. Salleo, Phys. Rev. B, 2005, **71**, 165202.

17. A. Salleo, R. J. Kline, D. M. DeLongchamp, M. L. Chabinyc, Adv. Mater., 2010, **22**, 3812.

18. Y. Kim, S. Cook, S. M. Tuladhar, S. A. Choulis, J. Nelson, J. R. Durrant, D. D. C. Bradley, M. Giles, I. McCulloch, C.-S. Ha, M. Ree, Nature Materials, 2006, **5**, 197.

19. H. Sirringaus, P. J. Brown, R. H. Friend, M. M. Nielsen, K. Bechgaard, B. M. W. Langeveld-Voss, A. J. H. Spiering, R. A. J. Janssen, E. W. Meijer, P. Herwing, D. M. DeLeeuw, Nature, 1999, **401**, 685.

20. H. Sirringaus, R. J. Wilson, R. H. Friend, M. Innbasekaran, W. Wu, E. P. Woo, M. Grell, D. D. C. Bradley, Appl. Phys. Lett., 2000, **77**, 406.

21. F. Pandiger, R. S. Rittberger, N. S. Sariciftci, Adv. Funct. Mater., 2003, **13**, 85.

22. G. Li, Y. Yao, H. Yang, V. Shrotriya, G. Yang, Y. Yang, Adv. Funct. Mater., 2007, **17**, 1636.

23. W. L. Wang, H. B. Wu, C. Y. Yang, C. Luo, Y. Zhang, J. W. Chen, Appl. Phys. Lett., 2007, **90**, 183512.

24. A. Ng, X. Liu, , C. H. To, A. B. Djurišić, J. A Zapien, W. K. Chan, ACS Appl. Mater. Interfaces, 2013,**5**(10), 4247.

25. P. A. Staniec, A. J. Parnell, A. D. F. Dunbar,H. Yi, A. J. Pearson, T. Wang, P. E. Hopkinson, C. Kinane, R. M. Dalgliesh, A. M. Donald, A. J. Ryan, A. Iraqi,R. A. L. Jones, A. L. Richard, D. G. Lidzey, Adv. Energ. Mater. 2011, **1**, 499.

26. F. Liu, Y. Gu, J. W. Jung, W. H. Jo, T. P. Russell, Journal of Polymer Science Part B: Polymer Physics, 2012, **50**, 1018.

27. A. J. Ward, A. Ruseckas, I. D. W. Samuel, J. Phys. Chem. C, 2012**, 116** (45), 23931.

28. H.-W. Wang, E. Pentzer, T. Emrick, T. P. Russell, ACS Macro Lett., 2014,**3**(1), 30.

29. J.-H. Kim, H. U. Kim, I.-N. Kang, S. K. Lee, S.-J. Moon, W. S. Shin, D.-H Hwang, Macromolecules, 2012**, 45** (21), 8628.

30. J. Liu, Q. Liang, H. Wang, M. Li, Y. Han, Z. Xie, L. Wang., J. Phys. Chem. C, 2014**, 118** (9), 4585.

31. N. E. Widjonarko, P. Schulz, P. A. Parilla , C. L. Perkins, P. F. Ndione , A. K. Sigdel , D. C. Olson, D. S. Ginley, A. Kahn, M. F. Toney, Joseph J. Berry, Adv. Energy Mater., 2014, **4**, 1301879.

32. B. Reeja-Jayan, T. Adachi, R. J. Ono, D. A Vanden Bout,C. W. Bielawski, A. Manthiram, J. Mater. Chem. A**,** 2013,**1**, 3258.

33. D. H. Wang, J. S. Moon, J. Seifter, J. Jo, J. H. Park, O. Ok. Park, A. J. Heeger, Nano Lett., 2011,**11**(8), 3163.

34. S. Kim, c.-h. Kim, S. K. Lee, J.-H. Jeong, J. Lee, S.-H. Jin, W. S. Shin, C. E. Song, J.-H. Choi, J.-R. Jeong, Chem. Commun. 2013, **49**, 6033.

35. Y. Sun, J. H. Seo, C.-J. Takacs, J. Seifter, A. J. Heeger, Adv. Mater. 2011, **23**, 1679.

36. S. Schumann, R. Da Campo, B. Illy, A. C. Cruickshank, M. A. McLachlan, M. P. Ryan, D. J. Riley, D. W. McComb, T. S. Jones, J. Mater. Chem., 2011, **21**, 2381.

37. H. Schmidt, K. Zilberberg, S. Schmale, H. Flügge, T. Riedl, W. Kowalsky, Appl. Phys. Lett., 2010, **96**, 243305.

38. S. Trost, K. Zilberberg, A. Behrendt, A. Polywka, P. Görrn, P. Reckers, J. Maibach, T. Mayer, T. Riedl, Adv. Energy Mater. 2013, **3**, 1437.

39. M. T. Greiner, M.G. Helander, W.-M. Tang, Z.-B. Wang, J. Qiu, Z.-H. Lu, Nat. Mater. 2012, **11**, 76.

40. Z. Zhang, Y. Xiao, H-X. Wei, G.-F. Ma, S. Duhm, Y.-Q. Li, J.-X. Tang, Appl. Phys. Express, 2013, **6**, 095701.

41. M. T. Greiner; Z.-H. Lu; NPG Asia Materials, 2013, **5**, e55, doi:10.1038/am.2013.29.

42. M. T. Greiner, L. Chai, M. G. Helander, W.-M. Tang, Z.-H. and Lu, Adv. Funct. Mater., 2012, **22**, 4557.

43. M. Vasilopoulou, A. M. Douvas, D. G. Georgiadou, L. C. Palilis, S. Kennou, L. Sygellou, A. Soultati, I. Kostis, G. Papadimitropoulos, D. Davazoglou, P. Argitis, J. Am. Chem. Soc., 2012, **134**, 16178.

44. I. Kostis, N. Vourdas, G. Papadimitropoulos, A. Douvas, M. Vasilopoulou, N. Boukos,D. Davazoglou, *J. Phys. Chem. C* **2013**, *117*, 18013.

45. M. Vasilopoulou, D. Davazoglou, D.; Materials Science in Semiconductor Processing**,** 2013, **6**, 1196.

46. M. Vasilopoulou, A. Soultati, D. G. Georgiadou, T. Stergiopoulos, L. C. Palillis, S. Kennou, S.; N. . Stathopoulos, D. Davazoglou, J. Mater. Chem. A, 2014, **2**, 1738.

47. M. Vasilopoulou, L. C. Palilis, D. G. Georgiadou, A. M. Douvas, P. Argitis, S. Kennou, L. Syggelou, G. Papadimitropoulos, I. Kostis, N. A. Stathopoulos, D. Davazoglou, Advanced Functional Materials, 2011, **21**, 1489.

48. G. Li, V. Shrotriya, Y. Yao, J. Huanga, Y. Yang, J. Mater. Chem., 2007, **17**, 3126

49. F. Padinger, R. S. Rittberger, N. S. Sariciftci, Adv. Funct. Mater., 2003, **13,** 85.

50. J. Ma, K. Hashimoto, T. Koganezawa, K. Tajima, Chem. Commun**.**, 2014, **50**, 3627.

51. A. M. Hiszpanski, Y.-L. Loo, Energy Environ. Sci.**,** 2014,**7**, 592.

52. U. Zhokhanets, T. Erb, G. Gobsch, M. Al-Ibrahim, O. Ambacher, Chem. Phys. Lett., 2006, **418**, 347.

53. T. Agostinelli, S. Lilliu, J. G. Labram, M. Campoy-Quiles, M. Hampton, E. Pires, J. Rawle, O. Bikondoa, D. D. C. Bradley, T. D. Anthopoulos, J. Nelson, J. E. Macdonald, Adv. Funct. Mater., 2011, **21**, 1701.

54. L. C. Palilis, M. Vasilopoulou, D. G Georgiadou, P Argitis, Organic Electronics, 2010, **11**, 887.

55. L. C. Palilis, M. Vasilopoulou, A. M. Douvas, D. G. Georgiadou, S. Kennou, N. A. Stathopoulos, V. Constantoudis, P. Argitis, Solar Energy Materials and Solar Cells, 2013, **114**, 205.

56. Y. Su, J. Seifter, M. Wang, L. A. Perez, C. Luo, C. G. Bazan, F. Huang, Y. Cao, A. J. Heeger, Adv. Energ. Mater., 2014, **4**, DOI: 10.1002/aenm.201301601.

57. P.K. Nayak, L. Barnea-Nehoshtan, R. S. Kim, A. Shu, G. Man, A. Kahn, D. Lederman, Y. Feldman, D. Cahen, Energy Environ. Sci., 2013, **6**, 3272.

58. L.-L. Chua, J. Zaumseil, J-.F. Chang, E. C.-W. Ou, P. K.-H. Ho, H. Sirringhaus, R. H. Friend, Nature, 2005, **434**, 194.

59. M. He, M. Wang, C. Linb, Z. Lin, Nanoscale**,** 2014, **6**, 3984.

60. N. C. Miller, S. Sweetnam, E. T. Hoke, R. Gysel, C. E. Miller, J. A. Bartelt, X. Xie, M. F. Toney, M. D. McGehee, Nano Lett., 2012, **12**(3), 1566.

61. E. T. Hoke, K. Vandewal, J. A. Bartelt, W. R. Mateker, G. D. Douglas, R. Noriega, K. R. Graham, G. M. G. Frecher, A. Salleo, M. D. McGehee, Adv. Energ. Mater., 2012, **3**, 220.

62. G. Papadimitropoulos, N. Vourdas, K. Giannakopoulos, M. Vasilopoulou, D. Davazoglou, J. Appl. Phys., 2011, **109**, 103527.

63. N. Vourdas, G. Papadimitropoulos, I. Kostis, M. Vasilopoulou, D. Davazoglou, Thin Solid Films, 2012, **520**, 3614.

64. I. Kostis, N. Vourdas, M. Vasilopoulou, A. M. Douvas, G. Papadimitropoulos, N. Konofaos, A. Iliadis, D. Davazoglou, Thin Solid Films, 2013, **537**, 124.

Figure caption

Figure 1 Effect of metal oxides surface hydrogenation on P3HT:$PC_{71}BM$ blend film nanomorphology: (a), (d), (g), (j) XRD graphs, (b), (e), (h), (k) absorption spectra, (c), (f), (i), (l) refractive indices of the films deposited on metal (tungsten, molybdenum, titanium, zinc) oxides with low and high hydrogen content. (m) Illustration of the edge-on and face-on alignment of polymer chains in blend fils deposited on H-metal oxide surfaces via the formation of an extended interfacial hydrogen bonding network.

Figure 2 Device architecture and energy levels of metal oxides and photoactive blend bulk materials. Current density-voltage (J-V) characteristics of devices based on P3HT:$PC_{71}BM$ photoactive layer and different metal oxide substrates. Devices (b), (c) exhibit conventional arcitecture with (b) WO_x and OH-WO_x, (c) MoO_x and OH-MoO_x as hole selective interlayers. Devices (d), (e) exhibit reverse architecture with (d) ZnO and OH-ZnO, (e) TiO_2 and OH-TiO_2 as electron selective interlayers. Variation of (f) J_{sc} and (g) V_{oc} for P3HT:$PC_{71}BM$ based devices using metal oxide layers with low and high surface hydrogen content.

Figure 3 IPCE spectra of the solar cells based on P3HT:$PC_{71}BM$ photoactive layer and different metal oxide at the bottom electrodes.

Figure 4 Transient photocurrent measurements for OSCs based on P3HT:$PC_{71}BM$ photoactive blend and different metal oxides substrates near the maximum power point (500 mV) at room temperature.

Figure 5 The integrated photocurrent as a function of time for the four type of P3HT:$PC_{71}BM$ based OSCs.

Figure 6 Effect of metal oxide surface hydrogenation on PCDTBT:$PC_{71}BM$ blend films nanomorphology: (a), (d), (e), (g) XRD graphs, and (b), (c), (e), (h) absorption spectra, of the films deposited on metal (tungsten, molybdenum, titanium, zinc) oxides with low and high hydrogen content.

Figure 7 (a), (c), (e), (g) Current density-voltage (J-V) characteristics of devices based on PCDTBT:$PC_{71}BM$ photoactive layer and tungsten, molybdenum, zinc and titanium oxides at botom electrodes, respectively. (b), (d), (f), (h) The corresponding IPCE spectra of the same cells.

Figures

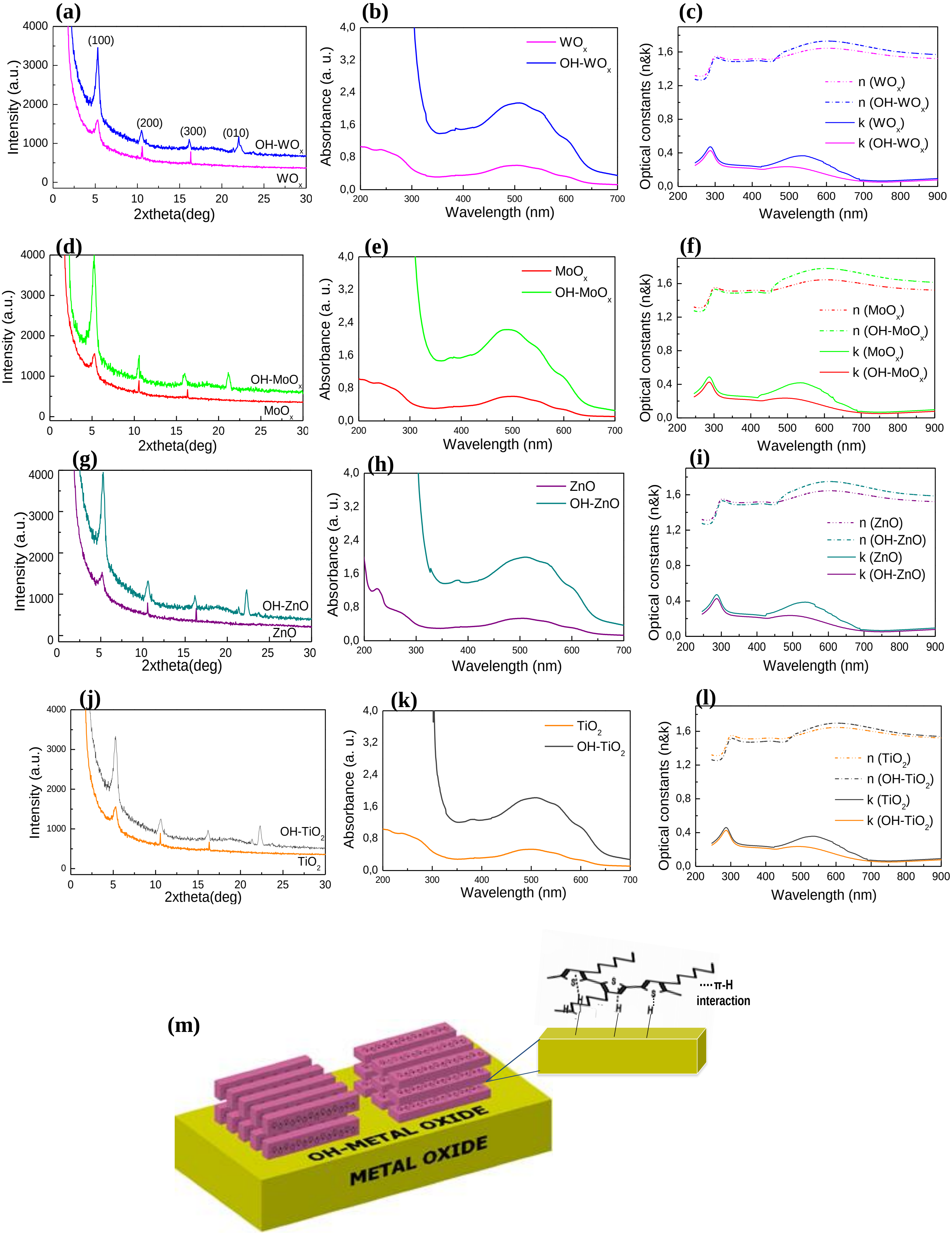

Figure 1

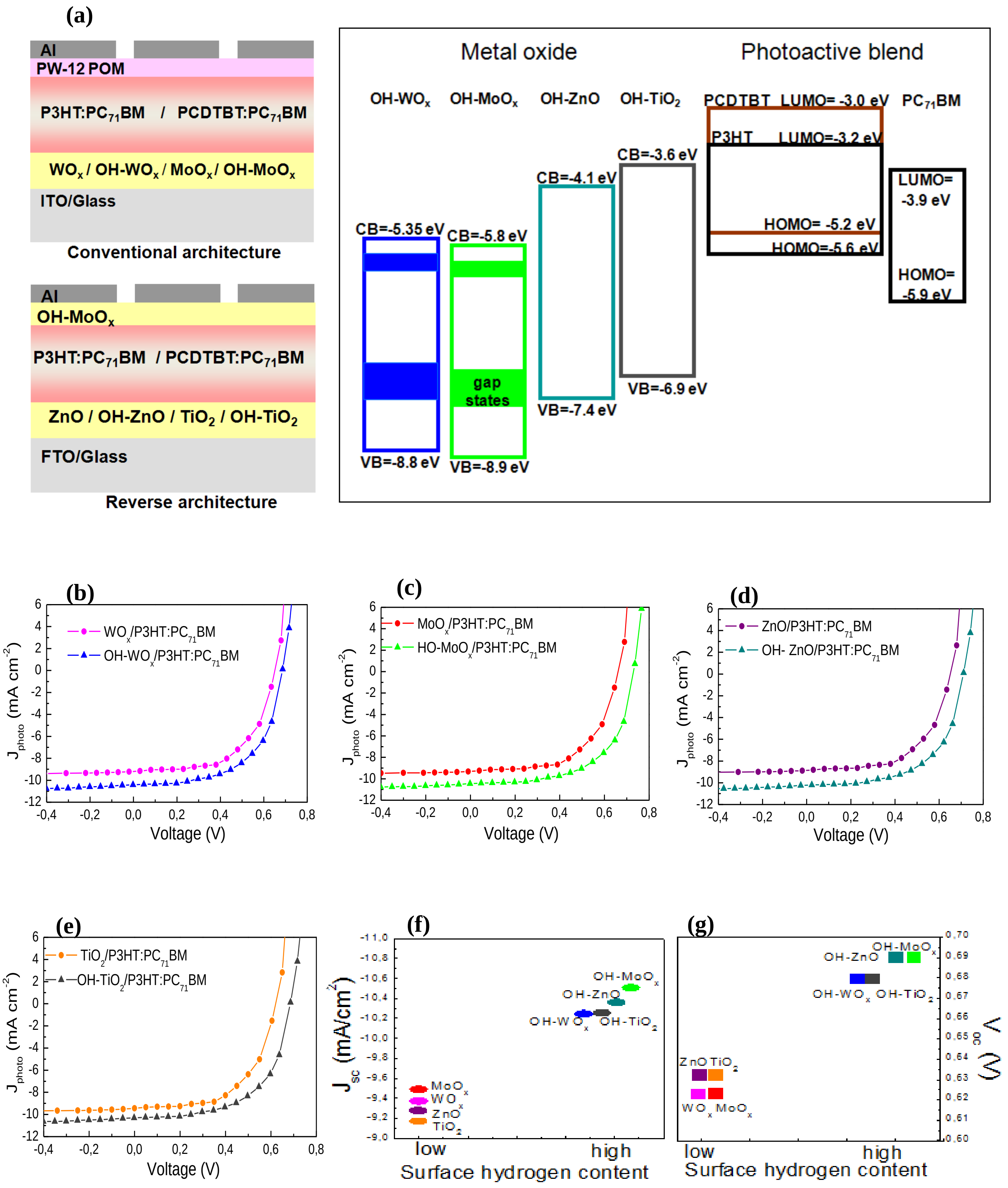
(a)
Al
PW-12 POM
P3HT:PC$_{71}$BM / PCDTBT:PC$_{71}$BM
WO$_x$ / OH-WO$_x$ / MoO$_x$ / OH-MoO$_x$
ITO/Glass
Conventional architecture
Al
OH-MoO$_x$
P3HT:PC$_{71}$BM / PCDTBT:PC$_{71}$BM
ZnO / OH-ZnO / TiO$_2$ / OH-TiO$_2$
FTO/Glass
Reverse architecture
Metal oxide
Photoactive blend
OH-WO$_x$
OH-MoO$_x$
OH-ZnO
OH-TiO$_2$
PCDTBT LUMO= -3.0 eV
PC$_{71}$BM
P3HT LUMO=-3.2 eV
CB=-3.6 eV
CB=-4.1 eV
CB=-5.35 eV
CB=-5.8 eV
LUMO= -3.9 eV
HOMO= -5.2 eV
HOMO=-5.6 eV
HOMO= -5.9 eV
gap states
VB=-6.9 eV
VB=-7.4 eV
VB=-8.8 eV
VB=-8.9 eV
(b)
WO$_x$/P3HT:PC$_{71}$BM
OH-WO$_x$/P3HT:PC$_{71}$BM
(c)
MoO$_x$/P3HT:PC$_{71}$BM
HO-MoO$_x$/P3HT:PC$_{71}$BM
(d)
ZnO/P3HT:PC$_{71}$BM
OH- ZnO/P3HT:PC$_{71}$BM
(e)
TiO$_2$/P3HT:PC$_{71}$BM
OH-TiO$_2$/P3HT:PC$_{71}$BM
J$_{photo}$ (mA cm^{-2})
Voltage (V)
6 4 2 0 -2 -4 -6 -8 -10 -12
-0,4 -0,2 0,0 0,2 0,4 0,6 0,8
(f)
J$_{sc}$ (mA/cm^2)
-11,0 -10,8 -10,6 -10,4 -10,2 -10,0 -9,8 -9,6 -9,4 -9,2 -9,0
OH-MoO$_x$
OH-ZnO
OH-WO$_x$
OH-TiO$_2$
MoO$_x$
WO$_x$
ZnO
TiO$_2$
low
high
Surface hydrogen content
(g)
V$_{oc}$ (V)
0,70 0,69 0,68 0,67 0,66 0,65 0,64 0,63 0,62 0,61 0,60
OH-MoO$_x$
OH-ZnO
OH-WO$_x$
OH-TiO$_2$
ZnO TiO$_2$
WO$_x$ MoO$_x$
low
high
Surface hydrogen content

Figure 2

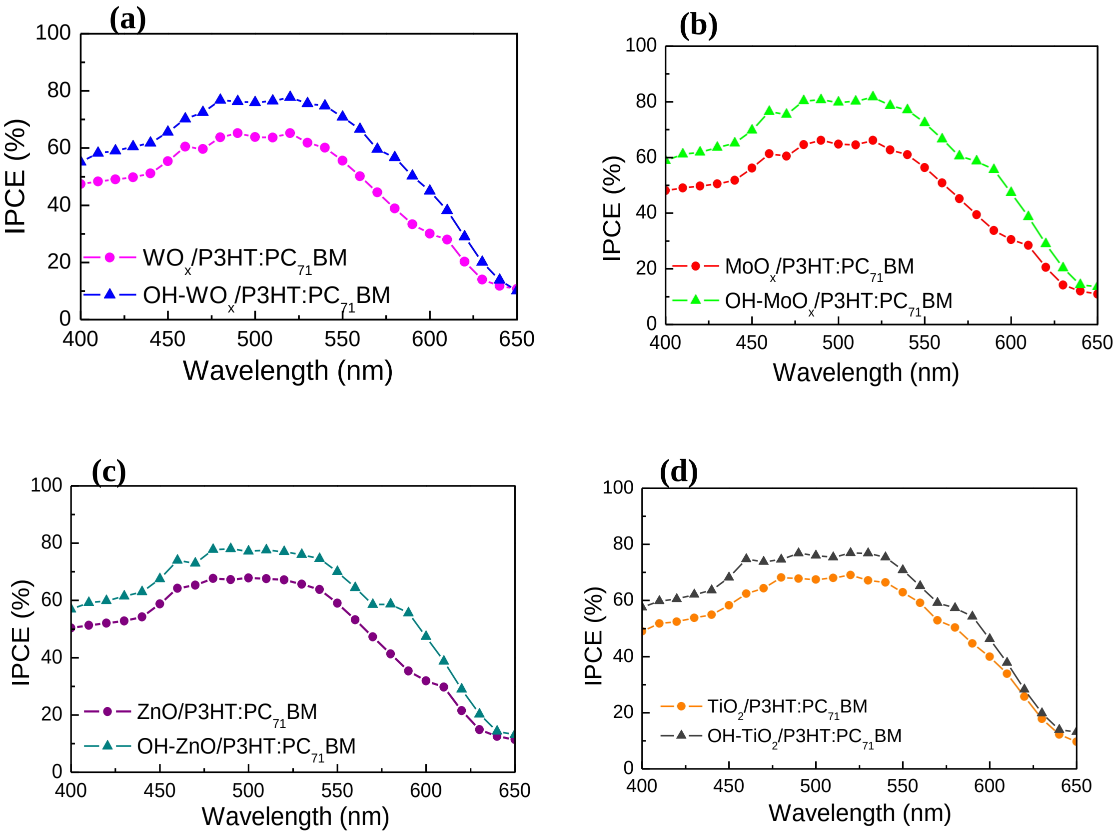

Figure 3

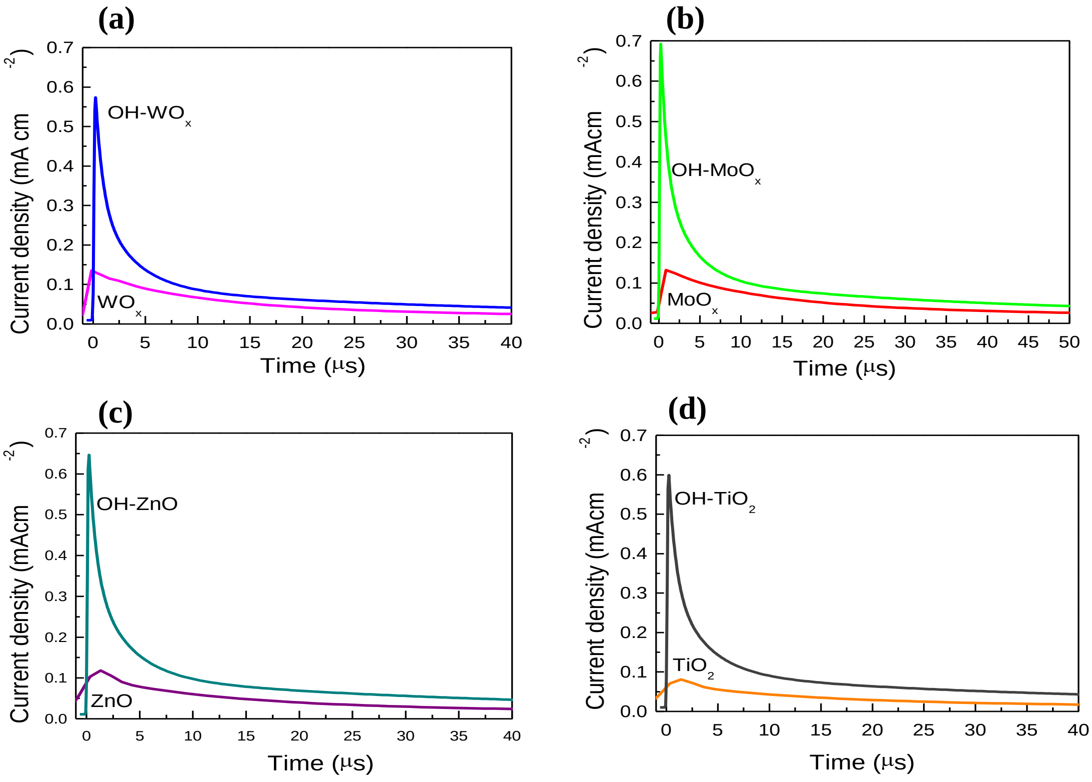

Figure 4

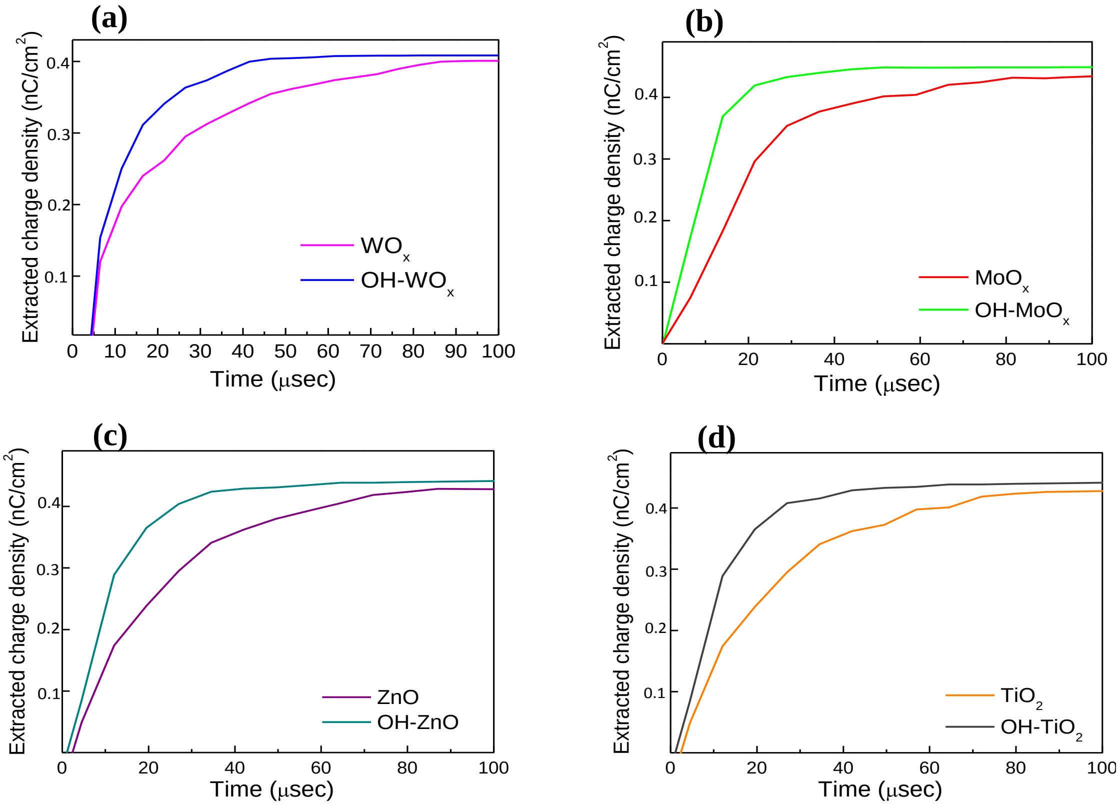
(a)
Extracted charge density (nC/cm^2)
0.1
0.2
0.3
0.4
0
10
20
30
40
50
60
70
80
90
100
Time (μsec)
WO$_x$
OH-WO$_x$
(b)
Extracted charge density (nC/cm^2)
0.1
0.2
0.3
0.4
0
20
40
60
80
100
Time (μsec)
MoO$_x$
OH-MoO$_x$
(c)
Extracted charge density (nC/cm^2)
0.1
0.2
0.3
0.4
0
20
40
60
80
100
Time (μsec)
ZnO
OH-ZnO
(d)
Extracted charge density (nC/cm^2)
0.1
0.2
0.3
0.4
0
20
40
60
80
100
Time (μsec)
TiO$_2$
OH-TiO$_2$

Figure 5

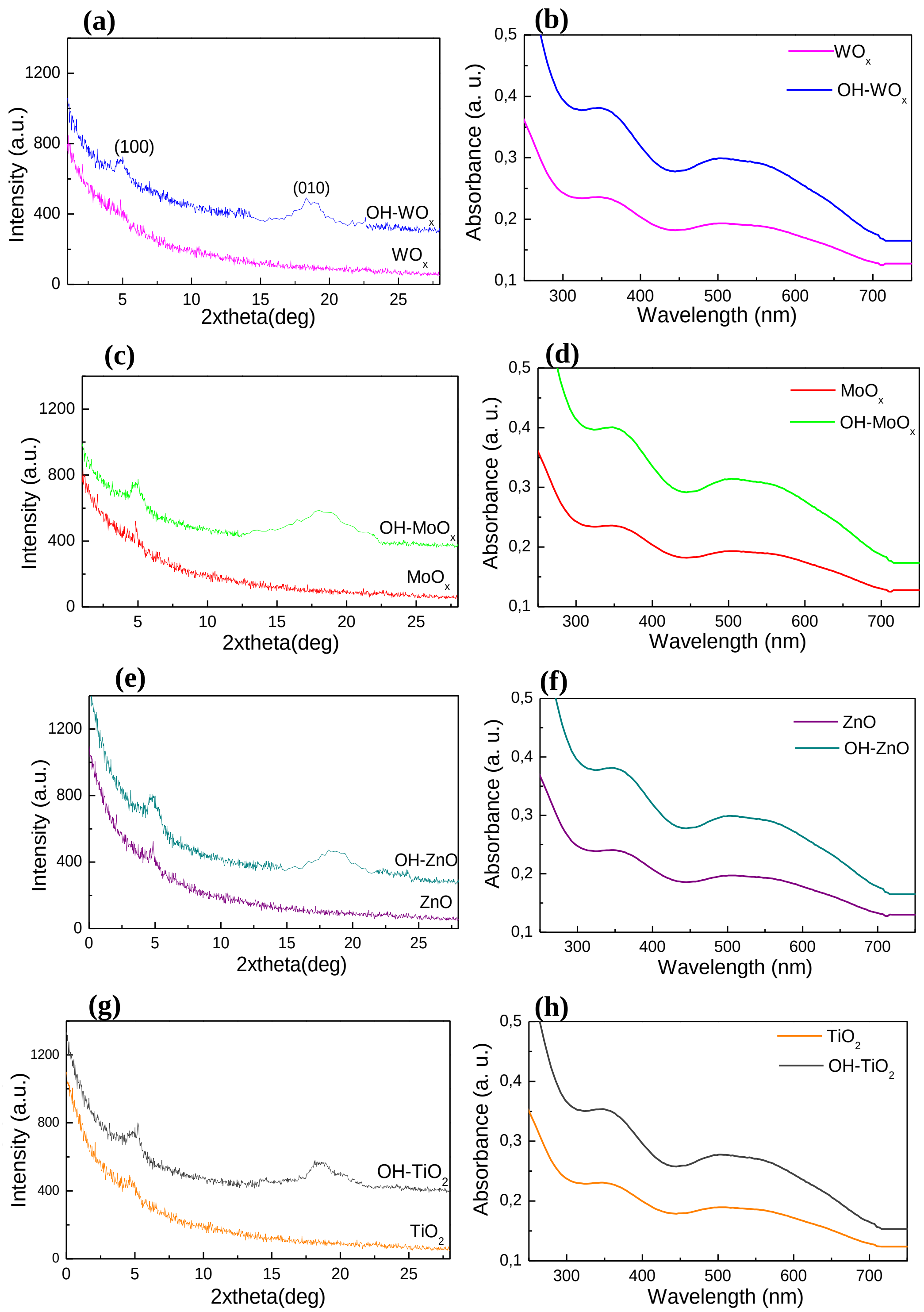
(a)
Intensity (a.u.)
2xtheta(deg)
0
400
800
1200
5
10
15
20
25
(100)
(010)
OH-WO_x
WO_x
(b)
Absorbance (a. u.)
Wavelength (nm)
0,1
0,2
0,3
0,4
0,5
300
400
500
600
700
WO_x
OH-WO_x
(c)
Intensity (a.u.)
2xtheta(deg)
OH-MoO_x
MoO_x
(d)
Absorbance (a. u.)
Wavelength (nm)
MoO_x
OH-MoO_x
(e)
Intensity (a.u.)
2xtheta(deg)
0
OH-ZnO
ZnO
(f)
Absorbance (a. u.)
Wavelength (nm)
ZnO
OH-ZnO
(g)
Intensity (a.u.)
2xtheta(deg)
OH-TiO_2
TiO_2
(h)
Absorbance (a. u.)
Wavelength (nm)
TiO_2
OH-TiO_2

Figure 6

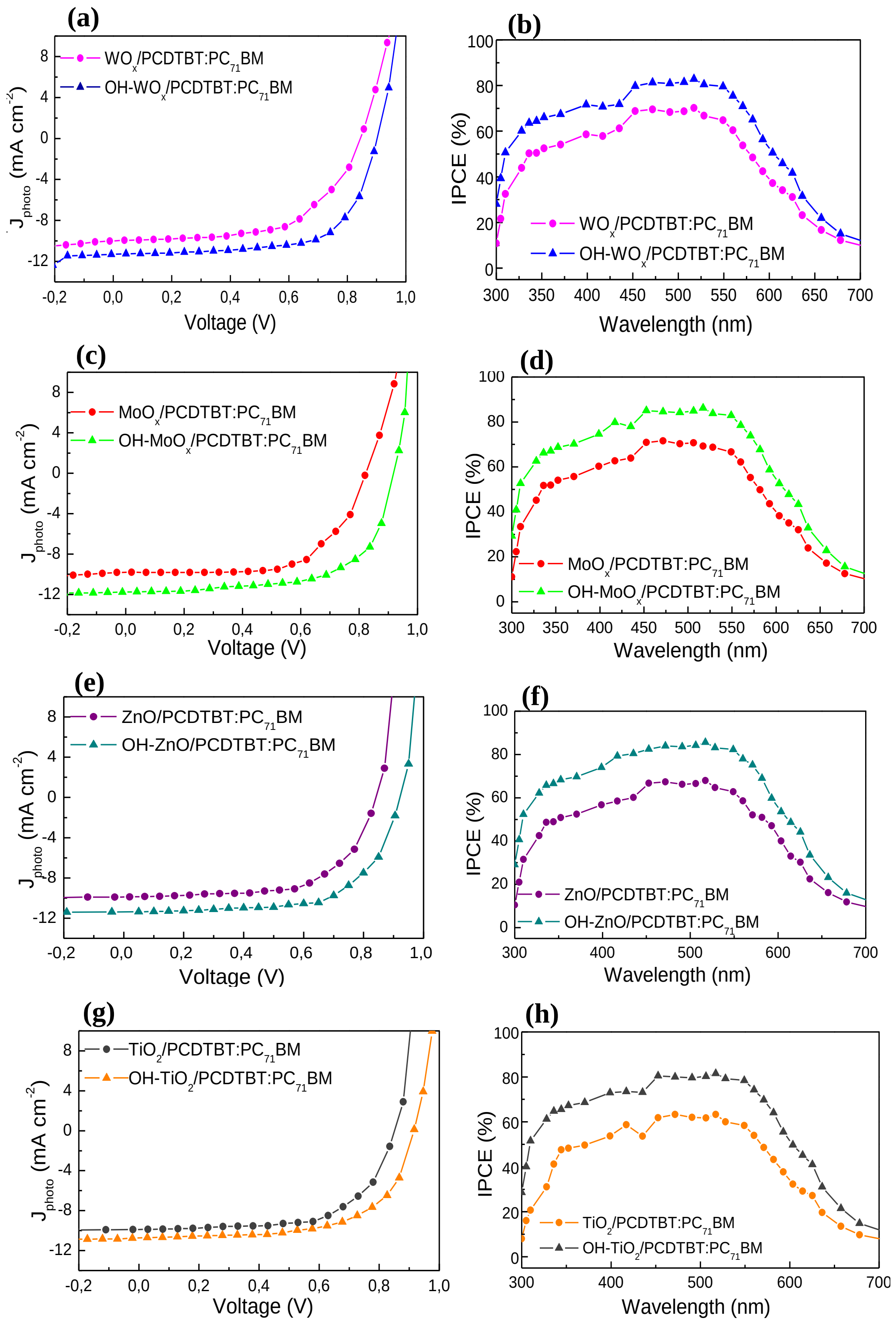
(a)
WO$_x$/PCDTBT:PC$_{71}$BM
OH-WO$_x$/PCDTBT:PC$_{71}$BM
J$_{photo}$ (mA cm^{-2})
8
4
0
-4
-8
-12
-0,2
0,0
0,2
0,4
0,6
0,8
1,0
Voltage (V)
(b)
IPCE (%)
100
80
60
40
20
0
300
350
400
450
500
550
600
650
700
Wavelength (nm)
WO$_x$/PCDTBT:PC$_{71}$BM
OH-WO$_x$/PCDTBT:PC$_{71}$BM
(c)
MoO$_x$/PCDTBT:PC$_{71}$BM
OH-MoO$_x$/PCDTBT:PC$_{71}$BM
J$_{photo}$ (mA cm^{-2})
Voltage (V)
(d)
IPCE (%)
Wavelength (nm)
MoO$_x$/PCDTBT:PC$_{71}$BM
OH-MoO$_x$/PCDTBT:PC$_{71}$BM
(e)
ZnO/PCDTBT:PC$_{71}$BM
OH-ZnO/PCDTBT:PC$_{71}$BM
J$_{photo}$ (mA cm^{-2})
Voltage (V)
(f)
IPCE (%)
Wavelength (nm)
ZnO/PCDTBT:PC$_{71}$BM
OH-ZnO/PCDTBT:PC$_{71}$BM
(g)
TiO$_2$/PCDTBT:PC$_{71}$BM
OH-TiO$_2$/PCDTBT:PC$_{71}$BM
J$_{photo}$ (mA cm^{-2})
Voltage (V)
(h)
IPCE (%)
Wavelength (nm)
TiO$_2$/PCDTBT:PC$_{71}$BM
OH-TiO$_2$/PCDTBT:PC$_{71}$BM

Figure 7

TOC graphic

Polymer blend solar cells exhibit improved nanomorphology and charge generation when deposit on metal oxides with high surface hydrogen content.